# Growth, Structure, and Evaluation of Laser Properties of $LiYb(MoO_4)_2$ Single Crystal

V. Volkov,[†] C. Cascales,[†] A. Kling,[‡] and C. Zaldo*,[†]

*Instituto de Ciencia de Materiales de Madrid, Consejo Superior de Investigaciones Científicas, c/ Sor Juana Inés de la Cruz 3, Cantoblanco, 28049 Madrid, Spain, and Instituto Tecnológico e Nuclear, Estrada Nacional No 10, 2686-953 Sacavém and Centro de Física Nuclear da Universidade de Lisboa, Av. Prof. Gama Pinto 2, 1649-003 Lisboa, Portugal*

*Received June 7, 2004. Revised Manuscript Received October 30, 2004*

Because of the incongruent melting of $LiYb(MoO_4)_2$ compound at 912 °C, $Li_2MoO_4$ and $Li_2Mo_2O_7$ fluxes have been used to nucleate single crystals of this compound. From the latter flux, crystals of about 1 $cm^3$ have been pulled by the top-seeded solution-growth method. Details on the preparation and growth procedures are provided. The Li concentration in the crystal has been assessed using $^7Li(p,\alpha)^4He$ nuclear reaction induced by protons. The [Yb]/[Li] molar composition ratio obtained in several samples is in the 1.01−1.05 range. This result compares well with the ratio [Yb]/[Li] = 1 expected from the above chemical formula, therefore nonextensive Li loss is experienced during the crystal growth. Polymorphic transformations to phases with symmetry lower than tetragonal have not been observed upon cooling. At room temperature the crystal structure shows the tetragonal space group $I\bar{4}$ (No. 82), with lattice parameters $a = 5.1191$ (9) Å and $c = 11.109$ (3) Å, $V = 291.11(10)$ Å$^3$, and $Z = 2$. This implies a high ytterbium density, namely [Yb] = $6.87 \times 10^{21}$ $cm^{-3}$. The optical absorption and photoluminescence properties are described in detail consistently with the anisotropic character of the tetragonal phase. The relative energies of the $Yb^{3+}$ Stark levels have been determined and the perspectives for applications as a laser material are evaluated.

## Introduction

The thickness reduction of laser crystal elements to the micrometer range for the so-called microchip (or thin disk) laser technology[1] requires the development and study of crystals with high density of optically active ions, typically in the $(2-5) \times 10^{21}$ $cm^{-3}$ range. Double tungstate and molybdate crystals with general formula $MRE(XO_4)_2$ (where M is a monovalent cation, RE is a trivalent rare earth, and $X = W^{6+}$ or $Mo^{6+}$) may achieve this RE concentration and they are presently attracting attention both as stimulated Raman shifters[2] and as RE-doped laser hosts.[3]

Yb lasers are considered an alternative to $Nd^{3+}$ lasers at $\lambda \approx 1.06$ $\mu$m, particularly when high ion concentration is required.[4] The strong concentration quenching of $Nd^{3+}$ limits the available Nd stoichimetric laser hosts to only a few, namely $NdP_5O_{14}$, Li(or K)$NdP_4O_{12}$, $Na_5Nd(WO_4)_4$, and $NdAl_3(BO_3)_4$.[5] However, $Yb^{3+}$ with only two multiplets, the ground $^2F_{7/2}$ multiplet and the excited $^2F_{5/2}$ one, has a very weak concentration quenching yield, very weak losses by up-conversion, and in comparison to $Nd^{3+}$ a reduced heat transfer to the lattice because of the lower energy mismatch between the pumping light and the fluorescence. For all these reasons $Yb^{3+}$ is very well suited for lasing in the infrared (IR) region, and it is also used for sensitizing other RE[6,7] and transition metal[8] ions.

It could be expected that a large number of stoichimetric Yb hosts produce laser action, however so far this has been shown only in $Yb_3Al_5O_{12}$ (YbAG)[9,10] and in $KYb(WO_4)_2$ (KYbW).[11] A reason for the scarce number of Yb stoichiometric laser hosts is that a weak crystal field on $Yb^{3+}$ leads to a low energy splitting of the Stark levels of the $^2F_{7/2}$ ground multiplet and therefore a significant thermal population of these Stark levels is found at 300 K. This situation limits the stimulated emission efficiency due to the increase of the

* Corresponding author. E-mail: cezaldo@icmm.csic.es.
[†] Instituto de Ciencia de Materiales de Madrid.
[‡] Instituto Tecnológico e Nuclear.

(1) Zayhowski, J. J.; Mooradian, A. *Opt. Lett.* **1989**, *14*, 24.
(2) Gallucci, E.; Goutaudier, C.; Bourgeois, F.; Boulon, G.; Cohen-Adad, M. Th. *J. Solid State Chem.* **2002**, *163*, 506.
(3) Kaminskii, A. A.; Gruber, J. B.; Bagaev, S. N.; Ueda, K.; Hömmerich, U.; Seo, J. T.; Temple, D.; Zandi, B.; Kornienko, A. A.; Dunina, E.; Pavlyuk, A. A.; Klevtsova, R. F.; Kuznetsov, F. A. *Phys. Rev. B* **2002**, *65*, 125108.
(4) Krupke, W. F. *IEEE J. Sel. Top. Quantum Electron.* **2000**, *6*, 1287.
(5) Chinn, S. R. In *Handbook of Laser Science and Technology*; Weber, M. J., Ed.; CRC Press: Boca Raton, FL, 1987; Vol I, pp 147−169.
(6) Strek, W.; Deren, P.; Bernarkiewicz, A. *J. Lumin.* **2000**, *87*−*89*, 999.
(7) Mateos, X.; Güell, F.; Pujol, M. C.; Bursukova, M. A.; Solé, R.; Gavaldà, Jna.; Aguiló, M.; Díaz, F.; Massons, J. *Appl. Phys. Lett.* **2002**, *80*, 4510.
(8) Choi, Y. G.; Kim, K. H.; Han, Y. S.; Heo, J. *J. Mater. Res.* **2000**, *15*, 278.
(9) aus der Au, J.; Spühler, G. J.; Südmeyer, T.; Paschotta, R.; Hövel, R.; Moser, M.; Erhard, S.; Karszewski, M.; Giesen, A.; Keller, U. *Opt. Lett.* **2000**, *25*, 859.
(10) Patel, F. D.; Honea, E. C.; Speth, J.; Payne, S. A.; Hutcheson, R.; Equall, R. *IEEE J. Quantum Electron.* **2001**, *37*, 135.
(11) Pujol, M. C.; Bursukova, M. A.; Güell, F.; Mateos, X.; Solé, R.; Gavaldà, Jna.; Aguiló, M.; Massons, J.; Díaz, F.; Klopp, P.; Griebner, U.; Petrov, V. *Phys. Rev. B* **2002**, *65*, 165121.

10.1021/cm049095k CCC: $30.25 
Published on Web 01/04/2005

threshold for population inversion and to the enhancement of losses by reabsorption of the emitted light. Therefore more work is required to develop new crystals with prospective properties for Yb lasing. The laser action of KYbW crystal stimulates the search among other members in the double molybdates and double tungstates families.

Double molybdates and double tungstates can be thought of as the substitution of two $Ca^{2+}$ ions in the tetragonal scheelite-type $CaWO_4$ by a couple of $M^+$ and $RE^{3+}$ ions, however the structural and physical properties of the resulting phase depend strongly on the radius of the considered M ion. Most of the K and Rb compounds undergo phase transitions upon slow cooling to room temperature from immediately below their melting or decomposition temperatures. These phase transitions are named polymorphic transformations and the resulting phases have symmetry lower than tetragonal, often monoclinic. Even though in these structures the trivalent RE occupy a single lattice site, multisite contributions have been disclosed.[12] In contrast, most Li and Na compounds retain tetragonal symmetry at 300 K, although some distortions with regards to the $I4_1/a$ (No. 88) scheelite space group appear. These could include twinning with monoclinic grains (the so-called $\beta'$ phase)[13] and loss of the inversion center of symmetry.[14] In these tetragonal structures the monovalent and trivalent (including RE) cations exhibit a short-distance random distribution leading to the multiple crystal fields on the RE sites and therefore broadening of the RE optical features. Moreover, in some of the tetragonal compounds doped with the largest ionic radii lanthanides, $Pr^{3+}$ and $Nd^{3+}$, a local symmetry lower than that corresponding to the point symmetry of the crystal sites has been observed.[15,16] Therefore more work is required to achieve a comprehensive knowledge of RE double molybdate and double tungstate crystals.

Molybdates of $Li^+$ and RE in the RE = La−Lu series are known in $Li_8RE_2(MoO_4)_7$ and $LiRE(MoO_4)_2$ compositions.[17] Most of the members of this $LiRE(MoO_4)_2$ series maintain a tetragonal unit cell at temperatures ranging from melting point to 300 K. The *a* and *c* parameters of the tetragonal unit cell, and therefore the cell volume, decrease from La to Lu; also a relationship of double molybdate melting point with ionic radius of $RE^{3+}$ evidently exists.[17,18]

Attempts to prepare $LiRE(MoO_4)_2$ compounds have been very scarce, and the phase diagram of the $Li_2MoO_4$−$Yb_2(MoO_4)_3$ binary system has not yet been plotted in detail. Klevtsov and Kozeva synthesized the $LiYb(MoO_4)_2$ composition[18] and reported its melting at 900 °C, a tetragonal scheelite-type structure with unit cell parameters $a = 5.14$ Å and $c = 11.14$ Å ($Z = 2$), and the calculated density results $\rho_{cal} = 5.64$ gcm$^{-3}$. On the other hand, Mokhosoev et al.[19] reported $a = 5.120$ Å, $c = 11.10$ Å, and resulting $\rho_{cal} = 5.70$ gcm$^{-3}$. This inconsistency requires a careful revision of the crystal structure and the density evaluation. It is interesting to note that in the $xLi_2MoO_4$−$yEr_2(MoO_4)_3$ system two compositions with the *x*:*y* ratios equal to 4:1 and 1:1 crystallize,[19] despite the similar $Er^{3+}$ and $Yb^{3+}$ ionic radii, 0.96 and 0.94 Å, respectively. Therefore, the growth of $LiLn(MoO_4)_2$ was a priori uncertain.

The purpose of this work is to describe for the first time the successful preparation, by using the top-seeded solution-growth (TSSG) method, of $LiYb(MoO_4)_2$ single crystal, to ensure the composition and crystalline structure, and, with a view on possible laser applications, to determine the relevant physical properties in comparison to the above-mentioned stoichiometric Yb laser crystals.

## Experimental Techniques

Product synthesis and crystal growth attempts were made using Pt-crucibles and Kantal A1 or $Si_2Mo$ heating elements, respectively. The temperature was set with a resolution of ±0.2 °C using a Eurotherm 818P temperature controller.

Differential thermal analyses (DTA) were made in still air using a simultaneous TG/DTA (Stanton model STA 781). About 72 mg of compound was heated and cooled at 5−10 °C/min rate using $Al_2O_3$ as reference.

The density of our crystals was calculated as $\rho = 5.77 \pm 0.07$ g/cm$^3$ by immersion in distilled water with the help of a Mettler-Toledo balance; resolution 0.1 mg.

Standard room-temperature X-ray powder diffraction (XRPD) analyses of polycrystalline samples of Yb-containing prepared molybdates, i.e., $Yb_2(MoO_4)_3$ and $LiYb(MoO_4)_2$, were performed to test the purity (or crystal structure) of the grown crystal. XRPD patterns were measured using a Siemens Kristalloflex 810 generator, Cu Kα radiation ($\lambda = 1.540598$ Å) and a computer-controlled D-500 goniometer equipped with a graphite monochromator. $2\theta$ scans were made in the angular range of $20° \le 2\theta \le 80°$, with $\Delta 2\theta = 0.02°$ steps and a counting time of 2 s per step.

A prismatic colorless suitable single-crystal cut from the grown crystal was mounted on a Siemens SMART CCD diffractometer equipped with a normal focus, 3 kW sealed tube. A small single crystal was selected to reduce the possibility of collecting data corresponding to a twinned crystal. A summary of the fundamental crystal and refinement data is given in Table 1. Data were collected at room temperature over a hemisphere of the reciprocal space by a combination of three sets of exposures. Each set had a different $\varphi$ angle for the crystal and each exposure of 20 s covered 0.3° in $\omega$. The crystal-to-detector distance was 5.09 cm. Unit cell parameters were determined by a least-squares fit of 60 reflections with $I > 20\sigma(I)$. Neutral-atom scattering factors for all atoms were used, and anomalous dispersion corrections were applied.[20] All calculations were performed using the SHELXTL program,[21] and ATOMS software[22] was used for the structure graphic.

(12) Bausá, L. E.; Terrile, M. C.; van der Meulen, H. P.; Rubio, J.; Solé, R.; Aguiló, M.; Díaz, F.; García-Solé, J. *Opt. Mater.* **1999**, *13*, 27.
(13) Klevtsov, P. V.; Kozeeva, L. P.; Kharchenko, L. Yu. *Sov. Phys. Crystallogr.* **1976**, *20*, 732.
(14) Hanuza, J.; Haznar, A.; Maczka, M.; Pietraszko, A.; Lemiec, A.; van der Maas, J. H.; Lutz, E. T. G. *J. Raman Spectrosc.* **1997**, *28*, 953.
(15) Méndez-Blas, A.; Volkov, V.; Cascales, C.; Zaldo, C. *J. Alloys Compd.* **2001**, *323*−*324*, 315.
(16) Méndez-Blas, A.; Rico, M.; Volkov, V.; Cascales, C.; Zaldo, C.; Coya, C.; Kling, A.; Alves, L. C. *J. Phys.: Cond. Matter* **2004**, *16*, 2139.
(17) Mokhosoev, M. V.; Alekseev, F. P.; Butukhanov, V. L. *Double Molybdates and Tungstates*; Nauka: Moscow, 1981; p 135.
(18) Klevtsov, P. V.; Kozeeva, L. P. *Inorg. Mater.* **1969**, *5*, 1842.
(19) Mokhosoev, M. V.; Getman, E. I.; Alekseev, F. P. *Dokl. Akadem. Nauk SSSR* **1969**, *185*, 361.
(20) *International Tables for Crystallography*; Kynoch Press: Birmingham, U.K., 1974; vol. 4.
(21) *SHELXTL Version 6.10 Software Package;* Siemens Energy and Automation Inc. Analytical Instrumentation.
(22) ATOMS Version 5.1. Dowty, E. *A Computer Program for Displaying Atomic Structures*; 521 Hidden Valley Road, Kingsport TN 37663.

**Table 1. Crystal and Structure Refinement Data for $LiYb(MoO_4)_2$**

| | |
|---|---|
| formula weight | 499.85 |
| temperature (K) | 296(2) |
| wavelength (Å) | 0.71073 |
| crystal system | tetragonal |
| space group | $I\bar{4}$ |
| unit cell dimensions (Å) | $a = b = 5.1191$ (9)<br>$c = 11.109$ (3) |
| volume (Å$^3$) | 291.11 (10) |
| $Z$ | 2 |
| density (g/cm$^3$) calcd | 5.702 |
| experimental | $5.77 \pm 0.07$ |
| absorption coefficient (mm$^{-1}$) | 20.172 |
| F(000) | 442 |
| crystal size (mm) | $0.15 \times 0.09 \times 0.07$ |
| $\theta$ range for data collection (°) | 4.38 to 31.11 |
| limiting indices | $-6 \le h \le 7$,<br>$-7 \le k \le 5$;<br>$-16 \le l \le 14$ |
| reflections collected | 994 |
| independent reflections | 420 ($R_{int} = 0.0659$) |
| refinement method | full-matrix least-squares on $F^2$ |
| data/restraints/parameters | 420/0/30 |
| goodness-of-fit on $F^2$ | 0.938 |
| final R indices [$I > 2\sigma(I)$] | $R_1 = 0.0414$, $wR_2 = 0.0924$ |
| R indices (all data) | $R_1 = 0.0740$, $wR_2 = 0.0974$ |
| extinction coefficient | 0.23 (2) |
| largest diff. peak and hole (eÅ$^{-3}$) | 1.375 and −2.491 |

The composition analysis has been made by ion beam techniques. Rutherford backscattering (RBS) measurements were performed using 1.8 MeV $H^+$ ions from a 3.1 MeV van-de-Graaff accelerator at Sacavém. A surface barrier detector with a small solid angle (1.7 msr) located at 160° recorded the spectrum of the backscattered protons for verification of the concentration of the crystal constituents other than lithium. Moreover, the α-particles produced in the nuclear reaction between protons and lithium were detected by an annular surface barrier detector located at 180° with respect to the beam. The large solid angle (14 msr) allowed recording of α-particle spectra with sufficient statistics despite the low reaction cross section and atomic concentration of Li in the sample.

For optical measurements the crystals were oriented by Laue X-ray diffraction patterns, cut, and polished with diamond paste. Raman measurements at 300 K were recorded in a Renishaw Ramascope 2000 microspectrometer. Optical absorption (OA) measurements were made in a Varian spectrophotometer model Cary 5E ($\lambda = 200-3000$ nm) and in a Bruker spectrophotometer model IFS 66v/S ($\lambda = 1.3-200\ \mu$m). The sample temperature was varied in the range 10−300 K by using a He close-cycle Oxford cryostate equipped with the proper temperature controller. For polarized measurements the sample was inserted between a Glan−Taylor polarizer and a depolarizer sheet. The spectra are labeled as $\sigma$ (**E**⊥c,**H**∥c) or $\pi$ (**E**∥c,**H**⊥c) with **E** and **H** being the electric and magnetic field components of the light, respectively. Photoluminescence (PL) was excited with a Ti-sapphire laser, dispersed in a SPEX spectrometer ($f = 34$ cm), and measured with a 77 K cooled Ge photodiode (Stokes PL) or a cooled Hamamatsu R928 photomultiplier (anti-Stokes PL). The fluorescence lifetimes were measured with a Hamamatsu R2658P photomultiplier and a Lecroy 500 MHz oscilloscope. In this case the excitation was provided by the light pulses of an optical parametric oscillator, Spectra Physics model MOPO-730.

## Results and Discussion

**Synthesis and Crystal Growth.** $LiYb(MoO_4)_2$ powder was prepared by solid-state reaction in two steps (I and II). The initial products used were $Li_2CO_3$, $Yb_2O_3$, and $MoO_3$ with 99.9% and 99.99% purity. Intermediate $Li_2MoO_4$ and $Yb_2(MoO_4)_3$ phases were achieved in I, following the sequence

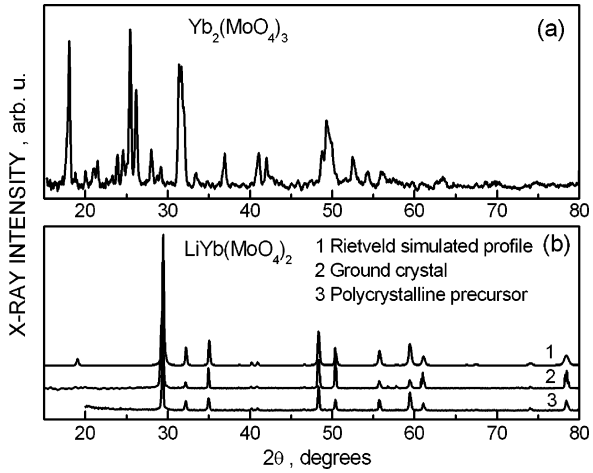


**Figure 1.** X-ray diffraction patterns of Yb-containing compounds prepared in steps I and II. (a) Polycrystalline precursor $Yb_2(MoO_4)_3$ synthesized at 1200 °C during 10 h. (b) Comparison between the Rietveld simulated profile and the XRPD patterns of ground $LiYb(MoO_4)_2$ crystals or polycrystalline synthesized $LiYb(MoO_4)_2$.

$$\text{(Ia)}\ Yb_2O_3 + 3MoO_3 \rightarrow Yb_2(MoO_4)_3$$
(annealed to $T = 900-1200$ °C for 10-20 h)

$$\text{(Ib)}\ Li_2CO_3 + MoO_3 \rightarrow Li_2MoO_4 + CO_2\uparrow$$
(annealed to $T = 460$ °C for 30 h)

and from these intermediate phases the final product was obtained in II by

$$\text{(II)}\ Li_2MoO_4 + Yb_2(MoO_4)_3 \rightarrow 2LiYb(MoO_4)_2$$
(annealed to $T = 840$ °C for 30 h)

Figure 1 shows the XRPD $\theta-2\theta$ scans obtained for the two Yb-containing phases, i.e., the initially prepared $Yb_2(MoO_4)_3$ and final $LiYb(MoO_4)_2$. By comparison to them, the crystal structure and phase purity of $LiYb(MoO_4)_2$ can be tested. XRPD patterns of the Ia products achieved after 20 h annealing to 500, 900, and 1200 °C are similar. These products are identified as $Yb_2(MoO_4)_3$, suggesting that the reaction Ia takes place even at moderated temperatures. The relative intensities found in the XRPD pattern of the powder achieved after reaction II agree with those expected from the Rietveld profile obtained on the basis of the $LiYb(MoO_4)_2$ structure determined later in the single crystal. This shows that $LiYb(MoO_4)_2$ is the only phase synthesized by reaction II and confirms previous results of Mokhosoev et al.[23] and Borchardt[24] on the thermal behavior of $M_2MoO_4-RE_2(MoO_4)_3$ mixtures, concluding that double molybdates can be formed by a relatively short time (4−15 h) annealing in the 600−1000 °C temperature range. Even lower synthesizing temperatures, i.e., $T = 300-500$ °C, were used, with the disadvantage of longer annealing times, i.e., $t = 100-200$ h.[25] Therefore, it is concluded that the formation of

(23) Mokhosoev, M. V.; Getman, E. I. *Zh. Neorgan. Khimii* **1969**, *14*, 2351.
(24) Borchardt, H. *J. Chem. Phys.* **1963**, *38*, 1251.
(25) Trunov, V. K.; Efremov, V. A. *Zh. Neorgan. Khimii* **1972**, *17*, 1167.

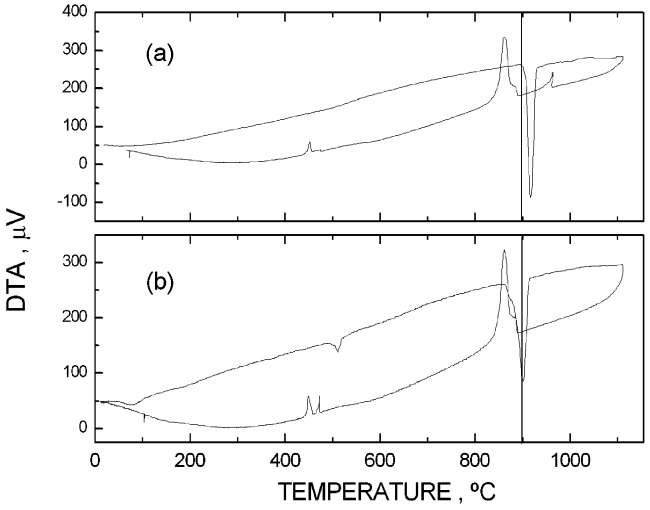


**Figure 2.** DTA analysis (10 °C/min) of $LiYb(MoO_4)_2$ single crystal. (a) First heating−cooling cycle with 1 h stop upon cooling at 960 °C. (b) Second heating−cooling cycle.

double lithium/RE molybdates with tetragonal structure can be easily carried out in a wide temperature range, $T = 300-1000$ °C.

Figure 2 shows the DTA analysis of $LiYb(MoO_4)_2$. In a first heating/cooling cycle (Figure 2a) only an endothermic peak is observed. The onset of this peak is at 900 °C and the peak maximum at 912 °C. The precise position of the peak slightly depends on heating/cooling rate and sample preparation (single crystal or powder) within ±5 °C. Hereafter we shall take 912 °C as a reference of the $LiYb(MoO_4)_2$ melting temperature. This peak corresponds to a solid−liquid transformation observed in crystal growth experiences. After 1 h of waiting at 960 °C upon cooling the DTA kinetics shows a complex re-solidification: a minor exothermic peak with onset at 900 °C is followed by a mayor one with onset at 875 °C, moreover another exothermic peak is present at 454 °C. In a second cycle (Figure 2b) an endothermic peak at about 500 °C is present and the major endothermic feature is broader than in the first cycle and it starts at lower temperature, i.e., 862 °C. These experimental findings suggest that $LiYb(MoO_4)_2$ melts at ≈912 °C with decomposition. $LiYb(MoO_4)_2$ decomposition was further confirmed by the presence of $Yb_2(MoO_4)_3$ X-ray reflections in the XRDP of the products of the re-solidified 26:74 molar % $Li_2MoO_4$/$LiYb(MoO_4)_2$ mixture.

The weak DTA peaks observed after $LiYb(MoO_4)_2$ melting in the 400−600 °C temperature range should be ascribed to products of the $LiYb(MoO_4)_2$ decomposition, although the contribution of reversible low-temperature phase transitions, characteristic of double molybdates with tetragonal structure,[26] cannot be completely excluded. Upon cooling, high-temperature polymorphic phase transitions to monoclinic crystal structures, like those found in most of the K-double tungstate, have not been observed in our $LiYb(MoO_4)_2$ crystals.

The incongruent melting of $LiYb(MoO_4)_2$ prevents the use of the Czochralski growth technique. We have used here a flux to grow $LiYb(MoO_4)_2$ single crystals. Dimolybdates of alkaline-earth ($M_2Mo_2O_7$) are acceptable solvents for growing of double molybdates.[27] Their advantages are as follows: (i) low melting point, for instance 530 °C for $Li_2Mo_2O_7$; (ii) weak dependence of the crystallization temperature of $LiYb(MoO_4)_2$ upon its concentration in the solvent, and (iii) common cations for solute and solvent that minimizes unwanted impurities. In most cases the optimal amount of scheelite-type compounds and solvent is in a 1:1 molar ratio.[17] Nevertheless, $Li_2MoO_4$ (mp 705 °C) has been also used as a flux for the growth of some scheelite-type molybdates.[28] For instance, like many other scheelite-type molybdates having either congruent or incongruent melting points, $BaMoO_4$ (mp 1480 °C) forms a simple eutectic phase diagram with $Li_2MoO_4$.[29] The same type of phase relationships can be preliminarily assumed between $LiYb(MoO_4)_2$ and $Li_2MoO_4$.

We have made attempts to grow $LiYb(MoO_4)_2$ single crystals from different starting mixtures, using $Li_2MoO_4$ (mp 705 °C) or $Li_2Mo_2O_7$ (mp 530 °C) fluxes. To realize a TSSG we have used seeds of scheelite-type $NaBi(WO_4)_2$ crystal (mp 875 °C) and a Pt wire. It is worth noting that despite the high-temperature melting (mp 1140 °C) of $NaLa(MoO_4)_2$ the use of this crystal as seed failed due to its dissolution in the starting melt.

Our first attempts to grow crystals using a $Li_2MoO_4$ flux have been undertaken using a 63:37 molar % $Li_2MoO_4$/$Yb_2(MoO_4)_3$ initial charge. The initial mixture (120 g) was heated in a platinum crucible up to 970 °C and kept at this temperature during 50 h. The spontaneous growth of crystals has been achieved by a slow cooling of the melt from 930 to 860 °C at the rate of 0.5 °C/h, followed by another cooling ramp at 1.4 °C/h rate between 860 and 720 °C. These spontaneously nucleated crystals have $\sim 3 \times 3 \times 5$ mm$^3$ dimensions and good transparency. Figure 1 shows the XRPD pattern of these crystals after grinding. The pattern shows the X-ray reflections of the $LiYb(MoO_4)_2$ phase. The minor intensity changes observed for some *hkl* reflections with regard to the Rietveld simulated pattern are likely due to texturing induced by the crystal cleavage plane.

Crystals with the $Li_8R_2(MoO_4)_7$ composition observed for instance in the cooling of $Li_2MoO_4$−$LiHo(MoO_4)_2$ and $Li_2MoO_4$−$LiEr(MoO_4)_2$ mixtures [29] do not appear in the binary $Li_2MoO_4$−$LiYb(MoO_4)_2$ system. This shows the simple eutectic character of the latter phase diagram which is sketched in Figure 3. The phase diagram, constructed on the basis of DTA and crystal growth experiences, shows the eutectic point at 670 °C and the $Li_2MoO_4$ melting at a temperature slightly larger but depending on the mixture composition. The $LiYb(MoO_4)_2$ melting for the different mixtures tested was likely a weak and broad feature observed by DTA, only clearly observed in the 45% $LiYb(MoO_4)_2$ composition. Above 54 molar % $LiYb(MoO_4)_2$ in the mixture the $LiYb(MoO_4)_2$ decomposition gives rise to $Yb_2(MoO_4)_3$ with a peritectic point at 913 °C.

(26) Savelieva, N. V.; Shakhno, I. V.; Plyuschev, V. E. *Izv. Akadem. Nauk SSSR, Neorg. Mater.* **1970**, *6*, 1665.
(27) Spitzin, V. I.; Trunov, V. K. *Dokl. Akad. Nauk SSSR* **1969**, *185*, 854.
(28) Chen, T. *J. Cryst. Growth* **1973**, *20*, 29.
(29) Mokhosoev, M. V.; Alekseev, F. P.; Lutzyk, V. I. *Diagrams of Molybdate and Tungstate Systems*; Nauka: Moscow, 1978; p 320.

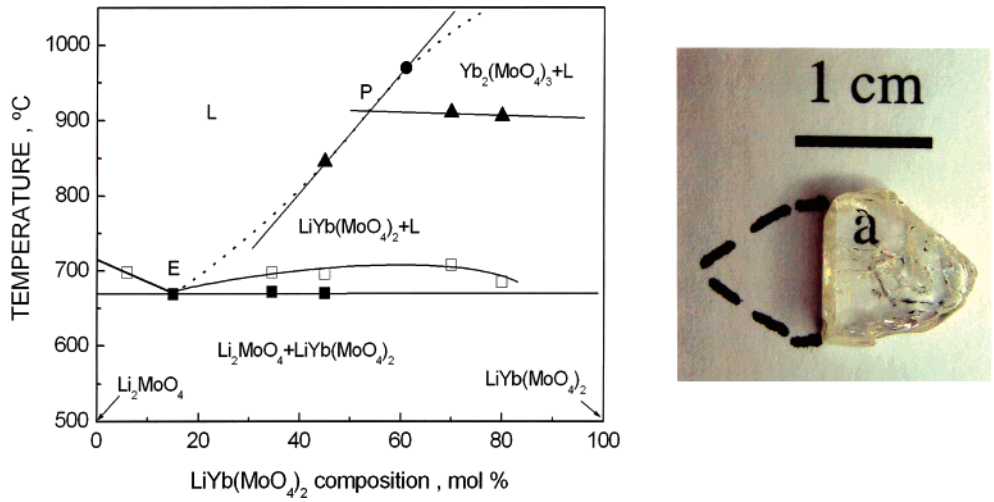


**Figure 3.** (Left) Phase diagram of $Li_2MoO_4/LiYb(MoO_4)_2$ mixture: ■,□,▲, DTA results; ●, crystal growth experience. (Right) Half of an *a*-cut crystal cross section. The dashed line shows approximately the as-grown crystal shape. The *c*-axis is in the horizontal direction.

Larger crystals with dimensions up to 12 mm have been grown by TSSG technique with a starting mixture containing $Li_2Mo_2O_7$ as flux. Three similar runs with initial charge of 50 molar % $LiYb(MoO_4)_2$ composition were undertaken with this flux. The starting mixture has been heated to 940 °C and kept at this temperature during 20 h. TSSG has been initiated at 910 °C, i.e., 2−5 °C below the $LiYb(MoO_4)_2$ decomposition temperature according to Figure 2. The crystal growth process was carried out by cooling the melt up to 780 °C at the rate of 0.5 °C/h with a 6 rpm rotating seed. When the grown crystal was withdrawn from the melt, the crystallization of the remaining flux was continued at the rate of 3 °C/h in the temperature range of 780−400 °C. Besides the crystals grown by TSSG method, resulting spontaneously nucleated crystals have been extracted from the solidified flux. The comparison of XRPD patterns of all crystalline samples studied shows that they belong to the tetragonal structure. It might be noted that the spontaneous crystals have more developed {110} facets than those grown by TSSG.

**Compositional Analysis.** Figure 4 shows the backscattered yield of $LiYb(MoO_4)_2$ single crystal under several experimental conditions. Figure 4a shows the RBS spectra of two samples from different TSSG runs and with different thicknesses (1 mm for sample 1 and 250 $\mu$m for sample 2) along with the fit achieved for the nominal crystal composition.

RBS is a very sensitive method to determine the concentration of elements with medium and large atomic numbers ($Z > 8$) in a sample, and thus the results of Figure 4a provide reliable Yb/Mo and O/Mo molar ratios, but RBS fails in the detection of lithium. Nuclear reaction analysis (NRA) can be used as an alternative ion beam method. The $^7Li(p,\alpha)^4He$ reaction[30] offers (due to the high abundance of $^7Li$ (92.5%) in natural Li) a convenient way for detection and has therefore been frequently applied.[31,32] This reaction has a high

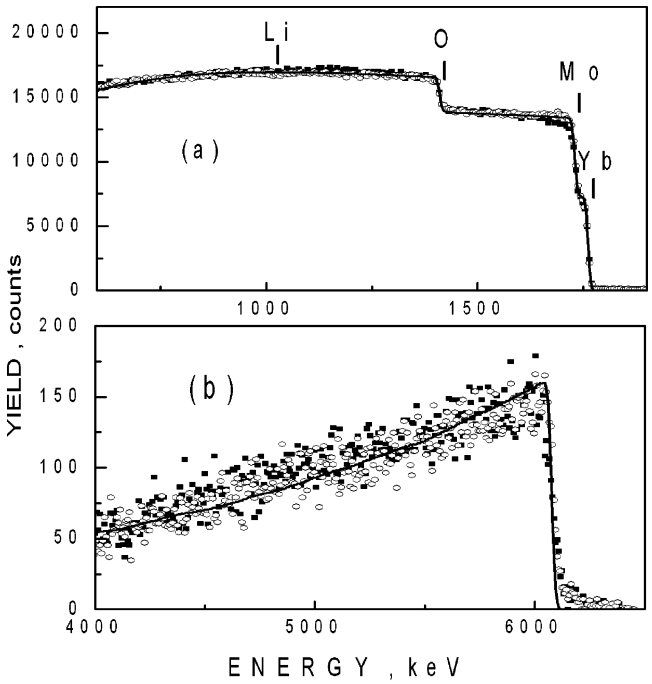


**Figure 4.** Ion beam analyses of $LiYb(MoO_4)_2$ samples. (a) RBS spectra of $LiYb(MoO_4)_2$ (points) and fit with RUMP software assuming the nominal composition (line). (b) $^7Li(p,\alpha)^4He$ nuclear reaction spectrum (points) and fit with the SENRAS code (line). Open symbols: sample 1, thickness 1 mm. Closed symbols: sample 2, thickness 250 $\mu$m.

positive $Q$ value ($Q = +17.4$ MeV) yielding two α-particles, each with an energy of about 6.1 MeV for the reaction with a 1.8 MeV proton. The high energy of the released α particles enables the study of the Li content in the material without any overlapping RBS signals from any of the other constituents.

Figure 4b shows the α-particle spectra recorded for the two $LiYb(MoO_4)_2$ crystals together with a simulation performed using the SENRAS code[33] assuming a stoichiometric composition of the samples. The program has a library of nuclear reactions to which new cross section sets can be added if necessary. A cross section file for the $^7Li(p,\alpha)^4He$ reaction, verified in the analysis of compounds of well-known

(30) Jeronymo, J. M. F.; Mani, G. S.; Sadeghi, A.; Forsyth, P. D. *Nucl. Instrum. Methods* **1962**, *33*, 449.
(31) Heck, D. *Nucl. Instrum. Methods B* **1988**, *30*, 486.
(32) Sagara, A.; Kamada, K.; Yamaguchi, S. *Nucl. Instrum. Methods B* **1988**, *34*, 465.
(33) Vizkelethy, G. *Nucl. Instr. Methods B* **1990**, *45*, 1.

**Table 2. Atomic Coordinates ($\times 10^4$) and Equivalent Isotropic Displacement Parameters ($Å^2 \times 10^3$) for $LiYb(MoO_4)_2$**

| | | *x* | *y* | *z* | OF[a] | *U*(eq)[b] |
|---|---|---|---|---|---|---|
| Yb(1) | 2*d* | 5000 | 0 | 2500 | 0.505 (6) | 7 (1) |
| Li(1) | 2*d* | 5000 | 0 | 2500 | 0.495 (6) | 7 (1) |
| Yb(2) | 2*b* | 5000 | −5000 | 0 | 0.512 (6) | 5 (1) |
| Li(2) | 2*b* | 5000 | −5000 | 0 | 0.488 (6) | 5 (1) |
| Mo(1) | 2*a* | 0 | 0 | 0 | | 4 (1) |
| Mo(2) | 2*c* | 0 | −5000 | 2500 | | 8 (1) |
| O(1) | 8*g* | 2456 (26) | −1493 (29) | 868 (14) | | 14 (3) |
| O(2) | 8*g* | 2480 (28) | −6614 (31) | 1660 (13) | | 15 (3) |

[a] Occupancy factor for the indicated site. They were refined with no restraints between 2*b* and 2*d* sites. [b] *U*(eq) is defined as one-third of the trace of the orthogonalized $U^{ij}$ tensor.

Li content and for the geometry used in this study, already existed. Best fits to the spectra have been obtained assuming Yb to $^7$Li ratios of 1:0.97 ± 0.08 and 1:0.93 ± 0.08 for samples1 and 2, respectively, which, taking into account the $^7$Li natural abundance, are equivalent to a total Yb:Li ratio of 1:1.05 ± 0.08 and 1:1.01 ± 0.08, respectively.

**Crystalline Structure.** Refinements of the $LiYb(MoO_4)_2$ structure have been performed in three tetragonal space groups (SG) commonly assumed in the literature of double molybdates and double tungstates, $I4_1$ (No. 80), $I4_1/a$ (No. 88),[34,35] and $I\bar{4}$ (No. 82),[14,36] with the same $I > 2\sigma$ reflections in the three cases. Whereas in the unit cells described by SG $I4_1/a$ and $I4_1$ Li and Yb atoms are sharing one crystal site, 4*b* or 4*a*, with $S_4$ or $C_2$ point symmetry respectively, in $I\bar{4}$ Li and Yb are almost statistically occupying two crystal sites, 2*b* and 2*d*, both with $S_4$ point symmetry. Since observed optical features of $LiYb(MoO_4)_2$ show a close dependence with the number and symmetry of occupied Yb site(s), in each case the final cycle of the full-matrix least-squares refinement included the corresponding occupancy factors (OF) for the crystal sites shared by Li and Yb. OF resulted to be 0.49(1)/0.51(1) and 0.510(3)/0.490(3) for Yb/Li in single positions 4*b* and 4*a* in $I4_1/a$ and $I4_1$ unit cells, respectively, leading to discrepancy factors of 0.073 and 0.044, respectively. However, since a few very weak reflections not authorized for these SGs were present in the total collected reflections, it was evident that only the SG $I\bar{4}$ can adequately describe the structure of $LiYb(MoO_4)_2$, and in fact, it allows establishment of Yb/Li OF values for the two 2*b* and 2*d* sites and simultaneously leads to positive values of the anisotropic thermal displacements for all atoms, with the lowest obtained discrepancy factor, 0.0414. Thus, corresponding $I\bar{4}$ final crystallographic data, atomic coordinates and occupancy factors for Yb and Li shared crystal sites, selected bonds and angles, and anisotropic displacement parameters for $LiYb(MoO_4)_2$ are given in Tables 1−4.

It is worth remarking that the OF values obtained by the X-ray refinement under SG $I\bar{4}$ assumption show a slight Yb enrichment leading to a total Yb:Li ratio of 1.034. This agrees with the Yb/Li composition ratio independently determined by NRA and gives full confidence to the OF calculation and SG selection. This agreement is not found when the SG $I4_1/a$ is assumed. Finally, our SG conclusion is similar to that found in the $AgYb(MoO_4)_2$ single crystals.[37]

**Table 3. Selected Bond Lengths (Å) and Angles (deg) for $LiYb(MoO_4)_2$**

| | | | |
|---|---|---|---|
| Yb/Li(1)−O(1) | 2.359 (14) × 4 | Li/Yb(1)−Mo(1) | 3.7768 (6) × 4 |
| Yb/Li(1)−O(2) | 2.35 (2) × 4 | Li/Yb(1)−Mo(2) | 3.6198 (6) × 4 |
| Yb/Li(2)−O(1) | 2.419 (14) × 4 | Li/Yb(2)−Mo(1) | 3.6198 (6) × 4 |
| Yb/Li(2)−O(2) | 2.40 (2) × 4 | Li/Yb(2)−Mo(2) | 3.7768 (6) × 4 |
| Mo(1)−O(1) | 1.76 (2) × 4 | Li/Yb(1)−Li/Yb(2) | 3.7768 (6) × 4 |
| Mo(2)−O(2) | 1.779 (14) × 4 | | |
| O(1)−Yb/Li(1)−O(1) | 126.2 (4) | O(1)−Yb/Li(2)−O(1) | 133.0 (8) |
| O(1)−Yb/Li(1)−O(1) | 79.6 (7) | O(1)−Yb/Li(2)−O(1) | 99.2 (3) |
| O(1)−Yb/Li(1)−O(2) | 152.7 (4) | O(1)−Yb/Li(2)−O(2) | 153.1 (4) |
| O(1)−Yb/Li(1)−O(2) | 68.4 (6) | O(1)−Yb/Li(2)−O(2) | 70.1 (6) |
| O(1)−Yb/Li(1)−O(2) | 73.8 (6) | O(1)−Yb/Li(2)−O(2) | 74.2 (5) |
| O(1)−Yb/Li(1)−O(2) | 76.1 (5) | O(1)−Yb/Li(2)−O(2) | 73.9 (6) |
| O(2)−Yb/Li(1)−O(2) | 133.3 (7) | O(2)−Yb/Li(2)−O(2) | 126.3 (4) |
| O(2)−Yb/Li(1)−O(2) | 99.0 (3) | O(2)−Yb/Li(2)−O(2) | 79.4 (7) |
| O(1)−Mo(1)-O(1) | 107.5 (5) | O(2)−Mo(2)-O(2) | 106.0 (5) |
| O(1)−Mo(1)-O(1) | 113.5 (9) | O(2)−Mo(2)-O(2) | 116.7 (10) |

**Table 4. Anisotropic Displacement Parameters ($Å \times 10^3$) for $LiYb(MoO_4)_2$[a]**

| | U11 | U22 | U33 | U23 | U13 | U12 |
|---|---|---|---|---|---|---|
| Yb/Li(1) | 7 (1) | 7 (1) | 8 (2) | 0 | 0 | 0 |
| Yb/Li(2) | 5 (1) | 5 (1) | 5 (2) | 0 | 0 | 0 |
| Mo(1) | 4 (1) | 4 (1) | 6 (1) | 0 | 0 | 0 |
| Mo(2) | 7 (1) | 7 (1) | 9 (2) | 0 | 0 | 0 |
| O(1) | 11 (8) | 9 (7) | 22 (7) | −7 (7) | 6 (6) | −2 (5) |
| O(2) | 27 (9) | 13 (7) | 6 (6) | −5 (7) | 7 (6) | 7 (6) |

[a] The anisotropic displacement factor exponent takes the form $-2\pi^2[h^2a^{*2}U^{11} + ... + 2hka^*b^*U^{12}]$.

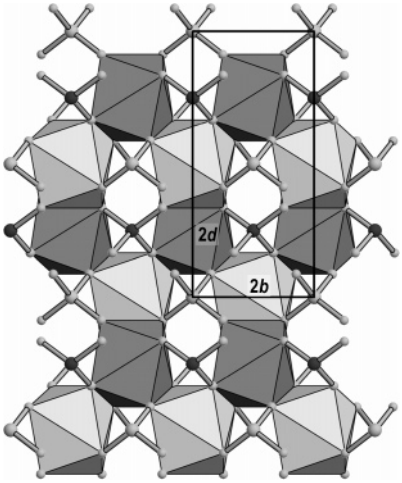


**Figure 5.** View of the $LiYb(MoO_4)_2$ structure in the *ac* plane. Larger light and dark spheres correspond to Mo(1) and Mo(2). Smaller spheres correspond to oxygens. $LiO_8$ and $YbO_8$ sharing edges polyhedra in *2b* and *2d* sites are connected by $MoO_4$ tetrahedra. The coordination around the *2b* and *2d* lattice sites of Li or Yb are shown as light and dark polyhedra, respectively.

The crystal structure contains two kinds of $MoO_4$ tetrahedra and $Yb/LiO_8$ distorted square antiprisms, see Figure 5. Along *a* and *b* directions it is built of parallel chains of alternate, sharing-edge $Yb/LiO_8$ and $MoO_4$ polyhedra, of only one type in each row, and in the *c* direction $Yb/LiO_8$ polyhedra from two different consecutive chains are linked through a common face, forming $(Yb/Li)_2O_{12}$ dimeric units.

For a later discussion, one feature that must be emphasized in this structure is that due to the random distribution of Yb

(34) Li, H.; Hong, G.; Yue, S. *Zhongguo Xitu Xuebau* **1990**, *8*, 37.
(35) Teller, R. G. *Acta Crystallogr. C* **1992**, *48*, 2101.
(36) Hanuza, J.; Benzar, A.; Haznar, A.; Maczka, M.; Pietraszko, A.; van der Maas, J. H. *Vib. Spectrosc.* **1996**, *12*, 25.
(37) Rath, M.; Müller-Buschbaum, Hk. *J. Alloys Compd.* **1993**, *198*, 193.

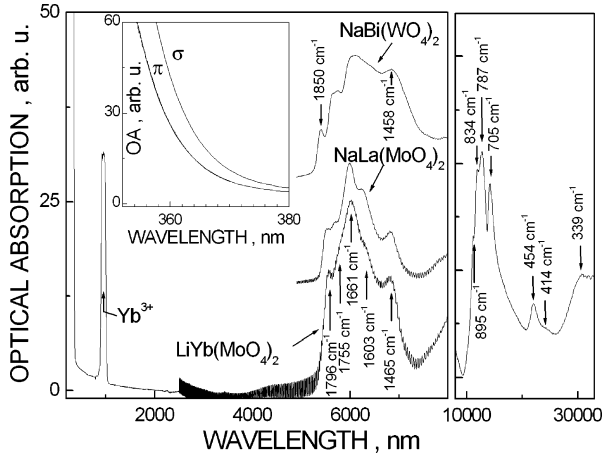


**Figure 6.** 300 K unpolarized optical absorption of $LiYb(MoO_4)_2$ single crystal. The inset shows the dicroism at the absorption edge. 300 K IR bands of $NaLa(MoO_4)_2$ and $NaBi(WO_4)_2$ are given for comparison. The UV−Vis−NIR spectra ($\lambda$ = 300−10 000 nm) are taken with ∼0.3-mm-thick plates and the far-IR spectra ($\lambda$ = 10−30 $\mu$m) is taken with powder dispersed in a KBr pellet.

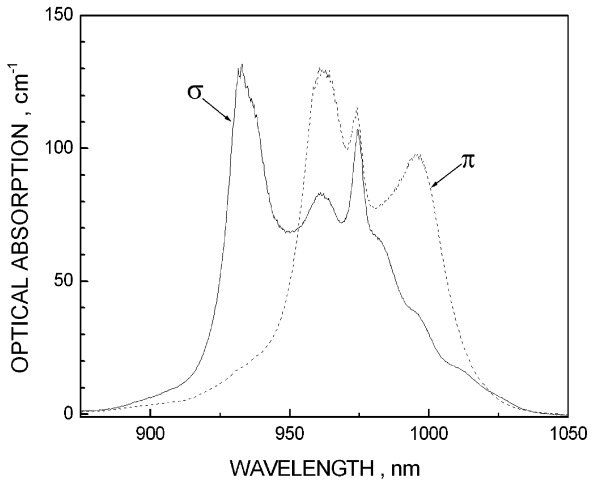


**Figure 7.** Polarized optical absorption of $LiYb(MoO_4)_2$ measured at 300 K.

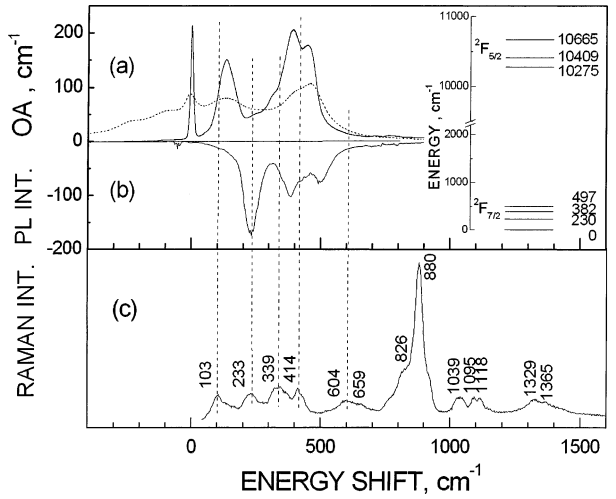


**Figure 8.** Comparison of the unpolarized optical properties of $LiYb(MoO_4)_2$ crystal. (a) Optical absorption at 9 K (solid line) and 300 K (dashed line). (b) Photoluminescence at 9 K, $\lambda_{exc}$ = 927 nm. In (a) and (b) $E_{zl}$ = 10 275 $cm^{-1}$ was taken as the energy origin. The inset shows the relative energy of $Yb^{3+}$ crystal field levels. (c) 300 K Raman spectrum.

cations over 2*b* and 2*d* sites, the shortest possible Yb−Yb distance (3.7768 Å) corresponds to the distance between two of these neighbor sites. Other relevant interionic distances and angles are summarized in Table 3.

**Optical Spectroscopy.** Figure 6 shows the 300 K transparency range of $LiYb(MoO_4)_2$ crystal. The ultraviolet (UV) absorption edge depends on the angle between the light polarization and the *c*-axis of the crystal (see Figure 6 inset), in agreement with the $S_4$ point symmetry of the lattice. The absorption edges obtained from a linear extrapolation of the stepping absorption are $\lambda_{th}$ = 363 nm for the $\pi$-spectrum and $\lambda_{th}$ = 365.5 nm for the $\sigma$-spectrum.

The $Yb^{3+}$ characteristic absorption is seen around $\lambda$ = 950 nm. The IR absorption edge is determined by the presence of several overlapped bands around $\lambda$ = 6000 nm (1796, 1755, 1661, 1603, and 1465 $cm^{-1}$). The shape and position of these IR bands are similar between molybdates, the case of $NaLa(MoO_4)_2$ is given for comparison. However, their positions differ from those observed in tungstates, the case of $NaBi(WO_4)_2$ is also given. In the latter case the energy difference between the lowest and highest energy bands is 60 $cm^{-1}$ larger than for molybdate crystals. These IR bands are mainly related with two-phonon $(MoO_4)^{2-}$ vibrations. At larger wavelengths in the far-infrared (far-IR, $\lambda$ > 10 000 nm) spectrum other bands due to one-phonon lattice vibrations are observed. The energies of the resolved vibration modes are 895, 834, 787, 705, 454, 414, and 339 $cm^{-1}$.

The dichroic character of the optical properties is also observed in the crystal field transitions of $Yb^{3+}$. Figure 7 shows the 300 K $\sigma$- and $\pi$-spectra corresponding to $^2F_{7/2}\rightarrow{}^2F_{5/2}$ $Yb^{3+}$ transitions. The OA spectrum of a randomly oriented sample can be obtained as a composition of these two spectra.

To determine the energies of the $^2F_{7/2}(n)$ and $^2F_{5/2}(n')$ Stark levels we have performed nonpolarized OA and PL measurements at 9 K. Moreover, Figure 8 shows the comparison of these spectra to the phonon energy spectrum derived from the 300 K Raman measurement, which will allow us to ascertain the vibronic nature of some of the observed sidebands. OA and PL spectra are represented with reference to the zero-line of the spectra, $^2F_{7/2}(0) \leftrightarrow {}^2F_{5/2}(0)$. This zero-line is observed in OA as a sharp line peaking at 10 275 $cm^{-1}$ ($\lambda$ = 973.1 nm). Another broader but well resolved band is observed in OA at 10 409 $cm^{-1}$ ($\lambda$ = 960.7 nm), and finally further overlapped bands are seen at 10 520 $cm^{-1}$ ($\lambda$ = 950.6 nm), 10 587 $cm^{-1}$ ($\lambda$ = 944.5 nm), 10 665 $cm^{-1}$ ($\lambda$ = 937.6 nm), and 10 721 $cm^{-1}$ ($\lambda$ = 932.7 nm).

It is worth noting that the temperature increase induces further optical absorption bands at energies lower than the zero-line transition, see the comparison with the 300 K OA in Figure 8a (dashed line). These latter bands are due to the population of $^2F_{7/2}(n \neq 0)$ Stark levels by thermal excitation. At 9 K these bands do not appear, therefore this effect can be excluded as the origin of the overlapped bands observed at 9 K in the 10 409−10 721 $cm^{-1}$ region of the OA spectrum. The coupling of the zero-line transition with Raman phonons (marked by the vertical dashed lines) does not match either of the positions of the 10 409−10 721 $cm^{-1}$ overlapped OA bands.

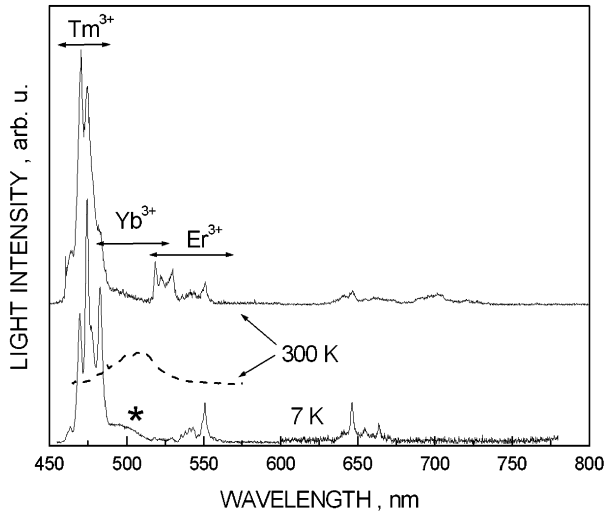


**Figure 9.** Anti-Stokes photoluminescence of $LiYb(MoO_4)_2$ crystal, $\lambda_{exc} = 927$ nm. The dashed line shows the IR $Yb^{3+}$ spectral distribution as a function of $\lambda/2$.

The most likely origin of the observed AO structure is the local vibrating environment of Yb. This has been observed also in other Yb lattices.[38] Taking into account that the overlapping induces some uncertainty on the actual position of the bands, a local Yb−O mode of about 60 $cm^{-1}$ may account for most of the structure in the Yb 9 K OA spectrum assuming that the three most prominent bands correspond to $^2F_{7/2}(0) \rightarrow {}^2F_{5/2}(n')$ transitions, i.e., $^2F_{5/2}(0) = 10\,275$ $cm^{-1}$, $^2F_{5/2}(1) = 10\,409$ $cm^{-1}$, and $^2F_{5/2}(2) = 10\,665$ $cm^{-1}$.

The 9 K PL shows three well-resolved bands. The zero-line emission, $^2F_{5/2}(0) \rightarrow {}^2F_{7/2}(0)$, is observed as a very weak band due to reabsorption. The other three emission bands peak at about 995.5, 1011, and 1022 nm. This provides the $^2F_{7/2}(n = 0, 1, 2, 3)$ energy positions as 0, 230, 382, and 497 $cm^{-1}$ respectively.

As a summary, Figure 8 shows a diagram of the crystal field energy levels of $Yb^{3+}$ in the $LiYb(MoO_4)_2$ lattice. Due to the 50% occupancy factors of Yb for the *2b* and *2d* sites, these levels must be understood as corresponding to an average Yb center accounting for the broadening caused by the different crystalline environments. The energy values determined here for the $^2F_{5/2}$ and $^2F_{7/2}$ Stark levels are consistent with the "barycentres law" developed for $Yb^{3+}$.[39]

Energy transfer from Yb to other residual RE impurities and cooperative up-conversion excitation of Yb−Yb pairs induce losses in the Yb stimulated emission process. The first mechanism can be avoided by a better purification, while the second is intrinsic to the considered lattice. Figure 9 shows the anti-Stokes PL achieved after excitation with infrared light at the $Yb^{3+}$ absorption, $\lambda = 927$ nm. Emissions are observed in the blue, green, and red spectral regions. The bands at 455−480 nm are characteristic of $^1D_2 \rightarrow {}^3F_4$ $Tm^{3+}$ photoluminescence,[40,41] while those in the region 510−563 nm correspond to $^2H_{11/2}+{}^4S_{3/2} \rightarrow {}^4I_{15/2}$ $Er^{3+}$ transitions.[42] In fact, the intensity enhancement observed around 550 nm upon cooling and the parallel intensity decrease of the 522 nm band is the behavior expected from the redistribution of the electron population of $^4S_{3/2}$ and $^2H_{11/2}$ levels of $Er^{3+}$. $^1G_4 \rightarrow {}^3F_4/{}^1D_2 \rightarrow {}^3F_{2,3}$ $Tm^{3+}$ and $^4F_{9/2} \rightarrow {}^4I_{15/2}$ $Er^{3+}$ transitions can contribute to the up-conversion observed between 640 and 700 nm. Only the feature marked as (*) around $\lambda = 500$ nm and seen in the relative scale of the figure as a weak band, could be associated to $Yb^{3+}$ cooperative excitation. This association is based on the rough matching with the wavelength halved spectral distribution of the $Yb^{3+}$ IR emission (dashed line).

Nevertheless, because of the Yb random distribution over the *2b* and *2d* sites about 90% of the Yb ions have at least another Yb in a neighboring *2b* or *2d* site, respectively, at a distance of 3.7768 Å. This distance is shorter than the minimum Yb−Yb distance required for an efficient cooperative up-conversion, namely <5 Å.[43] Other Yb−Yb distances in $LiYb(MoO_4)_2$ lattice can be initially ignored in this consideration as the near next distance corresponds to *2b*−*2b* (or *2d*−*2d*) sites at 5.1191 Å. Therefore, some intrinsic losses by Yb−Yb cooperative up-conversion seem not to be avoided. These losses can be minimized by finding a compromise between the Yb concentration (i.e., by slight substitution of Yb by Lu, the most similar in size, not optically active RE) and the dimension of the laser active element. While these losses are not desirable for lasing of $Yb^{3+}$, the presence of short Yb−RE distances will strongly enhance the efficiency of $Yb^{3+}$ as sensitizer of other lasants.

The reabsorption of the $Yb^{3+}$ emission gives rise to an artificial enlargement of the measured $^2F_{5/2}$ lifetime. This effect takes place even in thin plates, ~50 $\mu$m, in air due to the inner reflection of a significant fraction of the emitted light. To minimize this effect, the 300 K lifetime of the $^2F_{5/2}$ $Yb^{3+}$ multiplet was measured on $LiYb(MoO_4)_2$ single-crystal ground and dispersed in ethylene glycol (EG), moreover a large shift between the excitation ($\lambda_{EXC} = 930$ nm) and emission ($\lambda_{EMI} = 1060$ nm) wavelengths was used. The EG refractive index $n = 1.52$ reduces the fraction of emission trapped in the particles by inner reflection. We observed that the measured lifetime decreased for the lower $LiYb(MoO_4)_2$ concentration. Below 0.3 LYbMo/(EG+LYbMo) wt % no further decrease was observed, and the light decay fitted well a single exponential with a time constant $\tau = 183$ $\mu$s. This value is similar to those found in other double tungstate or double molybdate compounds, i.e., $\tau = 200$ $\mu$s in KYbW,[44] $\tau = 225$ $\mu$s in $Yb:NaLa(WO_4)_2$,[45] $\tau = 296$ $\mu$s in $Yb:NaBi(WO_4)_2$,[46] $\tau = 300$ $\mu$s in Yb:KYW,[47] $\tau = 320$ $\mu$s 1.5%Yb:$NaGd(WO_4)_2$, [48]and $\tau = 375$ $\mu$s in $Yb:KLu(WO_4)_2$.[49]

(38) DeLoach, L. D.; Payne, S. A.; Kway, W. L.; Tassano, J. B.; Dixit, S. N.; Krupe, W. F. *J. Lumin.* **1994**, *62*, 85.
(39) Haumesser, P. H.; Gaumé, R.; Viana, B.; Antic-Fidancev, E.; Vivien, D. J. *J. Phys. Cond. Matter* **2001**, *13*, 5427.
(40) Tu, C.; Li, J.; Zhu, Z.; Chen, Z.; Wang Y.; Wu, B. *Opt. Commun.* **2003**, *227*, 383.
(41) Güell, F.; Mateos, X.; Gavaldà, Jna.; Solé, R.; Aguiló, M.; Díaz, F.; Massons, J. *J. Lumin.* **2004**, *106*, 109.
(42) Rico, M.; Pujol, M. C.; Mateos, X.; Massons, J.; Zaldo, C.; Aguiló, M.; Díaz, F. *J. Alloys Compd.* **2001**, *323*−*324*, 362.
(43) Auzel, F.; Goldner, P. *Opt. Mater.* **2001**, *16*, 93.
(44) Pujol, M. C.; Bursukova, M. A.; Güell, F.; Mateos, X.; Solé, R.; Gavaldà, Jna.; Aguiló, M.; Massons, J.; Díaz, F.; Klopp, P.; Griebner U.; Petrov, V. *Phys. Rev B* **2002**, *65*, 165121.
(45) Serrano, M. D.; Esteban, F.; Zaldo, C. *J. Cryst. Growth*, accepted for publication.

**Table 5. Comparison of Optical Parameters Obtained at 300 K for $LiYb(MoO_4)_2$ Crystal with Those of Yb-doped $KGd(WO_4)_2$ (Yb:KGW), $KYb(WO_4)_2$ (KYbW), Yb-doped $Y_3Al_5O_{12}$ (Yb:YAG), and $Yb_3Al_5O_{12}$ (YbAG) Laser Hosts**

| | $LiYb(MoO_4)_2$[a] | Yb:KGW[b]/KYbW[c] | Yb:YAG[d]/YbAG[e] |
|---|---|---|---|
| $\sigma_{EXC}$ ($10^{-21}$ cm$^2$) | 15.4 ($\sigma$-, $\pi$-) | 120/117($N_m$),21($N_p$),16($N_g$) | 8/7 |
| $\lambda_{EXC}$ (nm) | 932($\sigma$-), 962 ($\pi$-) | 981/981 | 941/940 |
| $\sigma_{EMI}$ ($10^{-21}$ cm$^2$) | 14.7 ($\sigma$-) | 30 /20($N_m$), 15($N_p$), 3($N_g$) | 19 /23 |
| $\sigma_{reabsorp}$, ($10^{-21}$ cm$^2$) | 2 | 2.9/≈1 | 1.2/1.3 |
| $\lambda_{EMI}$ (nm) | 1011.8 | 1026($N_m$)/1025($N_m$,g),1040($N_p$) | 1031/1030 |
| $^2F_{5/2}$ lifetime ($\mu$s) | 183 | ≈300/200 | 950/664 |
| $^2F_{7/2}$ splitting (cm$^{-1}$) | 497 | 535/555 | 785/761 |
| $I_{sat}$ (kW/cm$^2$) | 77 ($\sigma$-) | 13/8.6 ($N_m$) | 28/45 |
| | 73 ($\pi$-) | | |
| $I_{min}$ (kW/cm$^2$) | 9.8 ($\sigma$-) | 0.15/≈0.5 ($N_m$) | 1.5/2.4 |
| | 9.3 ($\pi$-) | | |

[a] This work. [b] Ref 52. [c] Ref 44. [d] Ref 50. [e] Ref 10.

Let us now evaluate some parameters of interest for laser applications. $Yb^{3+}$ is considered as a quasi-four level system. Ignoring cavity losses, the two basic parameters to be compared with those of other Yb-lasing materials are the saturation intensity, $I_{sat}$, at the pumping wavelength, $\lambda_p$, and the minimum absorbed pump intensity that is required for transparency at the emission wavelength, $I_{min}$.[50]

The fraction of excited Yb ions is given by $I_{abs}/I_{sat}$, therefore low $I_{sat}$ values are required. $I_{sat}$ is given by $I_{sat} = hc/(\lambda_{EXC}\sigma_{EXC}\tau)$, where $\sigma_{EXC} = \alpha(\lambda_{EXC})/[Yb]$ is the absorption cross section at the excitation wavelength, $\lambda_{EXC}$, and $\tau$ is the radiative (or emission) lifetime of the $^2F_{5/2}$ multiplet. Two pumping wavelengths with similar absorption cross sections of $\sigma_{EXC} = 1.54 \times 10^{-20}$ cm$^2$ can be considered: $\lambda_{EXC} = 932$ nm for $\sigma$-polarized light and $\lambda_{EXC} = 962$ nm for $\pi$-polarized. Taking into account the $^2F_{5/2}$ fluorescence lifetime measured, $I_{sat}$ values summarized in Table 5 were calculated.

$I_{min}$ describes the minimum pump (or excitation) intensity required to achieve transparency at the laser emission wavelength. To allow a first comparison between Yb stoichiometric materials the expression $I_{min} = \beta_{min}I_{sat}$ (strictly only valid for low absorption conditions) was used, where $\beta_{min}(\lambda) = \sigma_{EXC}(\lambda)/[\sigma_{EMI}(\lambda) + \sigma_{EXC}(\lambda)]$.

The emission cross section can be calculated by the reciprocity principle[51] as

$$\sigma_{EMI}(E) = \sigma_{GSA}(E) \times (Z_l/Z_u) \times \exp[(E_{zl} - E)/k_BT]$$

where E is the light energy, $Z_l$ and $Z_u$ are the partition functions of the lower and upper levels, $Z = \sum_i d_i \exp(-E_i/k_BT)$ with $d_i$ being the level degeneracy. With the energy position ($E_i$) of the $Yb^{3+}$ levels in the ground and excited multiplets discussed previously, we arrive at $Z_l/Z_u = 0.943$.

Convenient conditions for lasing are likely encountered by pumping either at $\lambda = 932$ nm with $\sigma$-polarized light or at $\lambda = 962$ nm with $\pi$-polarized light. Figure 10 shows the

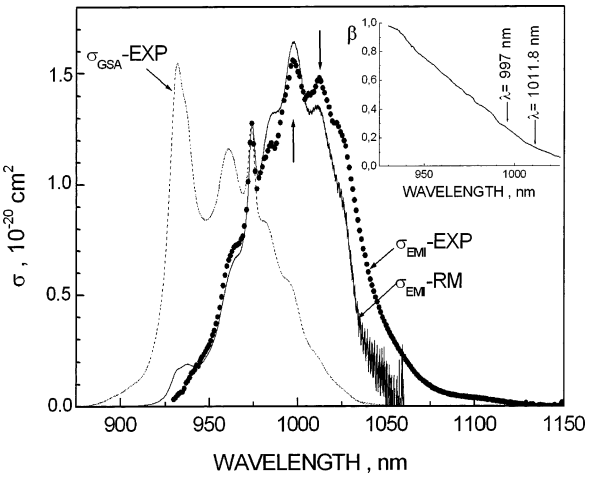


**Figure 10.** 300 K $\sigma$-polarized cross sections of $LiYb(MoO_4)_2$ crystal: experimental ground-state absorption cross section $\sigma_{GSA}$ (dashed line); calculated emission cross section $\sigma_{EMI}$-RM (solid line); normalized experimental emission cross section $\sigma_{EMI}$ (points). The inset shows the spectral dependence of $\beta$ and the expected free running wavelengths.

$\sigma$-polarized experimental 300 K $\sigma_{EXC}$ and the $\sigma_{EMI}$ values calculated by the reciprocity method. The latter is compared to the experimental $\sigma$-polarized $\sigma_{EMI}$. Although a thin (150 $\mu$m) sample was used to minimize reabsorption effects, the experimental emission band has been corrected by this effect and by the spectral response of the equipment, afterward it was normalized to the $\sigma_{EMI}$ calculated value at the zero-line wavelength. Given the uncertainty of the correction procedures, the matching between the experimental and calculated emission cross sections is good. The inset of Figure 10 shows $\beta_{min}(\lambda)$. A favorable extraction wavelength is $\lambda_{ext} = 1011.8$ nm, at this wavelength $\beta_{min} = 0.128$ and therefore $I_{min} \approx 9.5$ kW/cm$^2$ for the two excitation wavelengths considered.

Ignoring internal losses in the crystal, the laser gain condition can be expressed as $\beta\sigma_{EMI}(\lambda) - (1 - \beta)\sigma_{GSA}(\lambda)$, were $\beta$ represents the ratio of the excited state to total populations. Figure 11 shows possible spectral regions for lasing as a function of $\beta$. At first a $\pi$-configuration seems more efficient, however particular care must be taken to control emission reabsorption due to the high absorption in the 1000−1050 nm region in this configuration.

The comparison of the material properties summarized in Table 5 suggests that lasing of $LiYb(MoO_4)_2$ single crystals will require larger pumping threshold than that needed for $KYb(WO_4)_2$ or $Yb_3Al_5O_{12}$, but if losses were overcome $LiYb(MoO_4)_2$ would provide improved tuneability, better

(46) Rico, M. PhD Thesis, Universidad Autónoma de Madrid, 2003.
(47) Demidovich, A. A.; Kuzmin, A. N.; Ryabtse, G. I.; Danailov, M. B.; Strek, W.; Titov, A. N. *J. Alloys Compd.* **2000**, *300*−*301*, 238.
(48) Voron'ko, Yu K.; Zharikov, E. V.; Lis, D. A.; Sobol', A. A.; Subbotin, K. A.; Ushakov, S. N.; Shukshin, V. E.; Dröge, S. *Inorg. Mater.* **2003**, *39*, 1308.
(49) Mateos, X.; Petrov, V.; Aguiló, M.; Solé, R.; Gavaldá, J.; Massons, J.; Díaz, F.; Griebner, U. *IEEE J. Quantum Electron.* **2004**, *40*, 1056.
(50) DeLoach, L. D.; Payne, S. A.; Chase, L. L.; Smith, L. K.; Kway, W. L.; Krupe, W. F. *IEEE J. Quantum Electron.* **1993**, *29*, 1179.
(51) McCumber, D. E. *Phys. Rev.* **1964**, *136*, A954.
(52) Kuleshov, N. V.; Lagatsky, A. A.; Podlipensky, A. V.; Mikhailov, V. P.; Huber, G. *Opt. Lett.* **1997**, *22*, 1317.

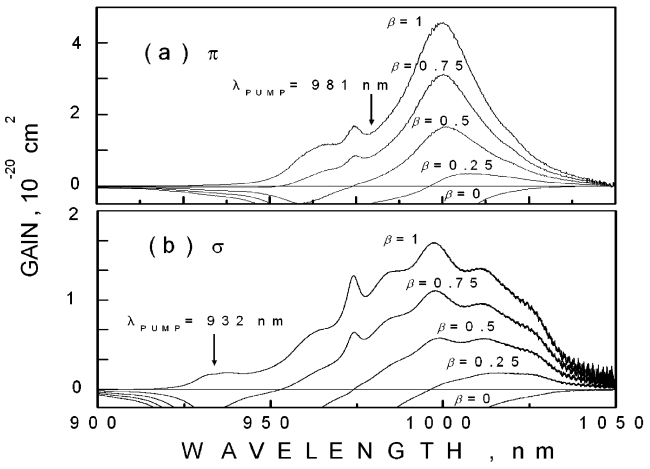


**Figure 11.** 300 K gain cross sections for $LiYb(MoO_4)_2$ crystal. The pump wavelength for each configuration is given as reference.

acceptance to diode pumping wavelength shifts, shorter pulse regime, and improved Yb−RE transfer rate.

## Conclusions

$LiYb(MoO_4)_2$ melts with decomposition at 912 °C preventing use of the Czochralski method for crystal growth. Single crystals of this compound have been nucleated and grown below the melting point using either $Li_2MoO_4$ or $Li_2Mo_2O_7$ fluxes. The properties of the crystals obtained are independent of the used flux. The Li composition of the crystals assessed by $^7Li(p,\alpha)^4He$ reaction was that corresponding to the compound formula and no trace of $Yb_2(MoO_4)_3$ phase was found. The crystal structure at 300 K is tetragonal with $Li^+$ and $Yb^{3+}$ ions sharing the same *2b* and *2d* lattice sites, whose occupancy factors close to 50% lead to a local stochastic cationic distribution around them. This structural disorder has two consequences: (i) multiple crystal fields on $Yb^{3+}$ ions giving rise to peak absorption and emission cross sections smaller than those observed in ordered double tungstate and double molybdate phases, and (ii) the presence of a large amount of Yb−Yb pairs lying at a short distance (3.7768 Å), for which in Yb laser processes likely leads to optical losses by cooperative excitation and some lifetime reduction. In comparison to the Yb-stoichiometric laser crystals so far demonstrated, this new Yb stoichiometric crystal promises laser action with larger bandwidth, but higher pump threshold intensity likely would be required.

**Acknowledgment.** Work supported by Ministerio de Ciencia y Tecnología under project MAT2002-4603-05-5 and by UE contract NMP3-CT-2003-505580. The GRICE (Portugal)−CSIC (Spain) cooperation agreement is gratefully acknowledged.

CM049095K